

## Distinguishing between the bi-stripe and Wigner-crystal model: A crystallographic study of charge-ordered $\text{La}_{0.33}\text{Ca}_{0.67}\text{MnO}_3$

Renhui Wang and Jianian Gui

*Department of Applied Science, Brookhaven National Laboratory, Upton, New York 11973  
and Department of Physics, Wuhan University, Wuhan 430 072, China*

Yimei Zhu\* and A. R. Moodenbaugh

*Department of Applied Science, Brookhaven National Laboratory, Upton, New York 11973  
(Received 24 November 1999)*

In order to resolve discrepancies in the charge-ordered structure between the Wigner-crystal and bi-stripe models,  $\text{La}_{0.33}\text{Ca}_{0.67}\text{MnO}_3$  was studied using quantitative electron diffraction and high-resolution imaging. Image simulations based on dynamic electron-diffraction theory suggest that the apparent difference in spacing between the  $\text{Mn}^{3+}\text{-Mn}^{3+}$  and  $\text{Mn}^{3+}\text{-Mn}^{4+}$  stripes, which is the basis of the bi-stripe model, can vary significantly with imaging conditions and may not directly represent the difference in actual spacing of atomic planes. Electron-diffraction study of crystal regions far away from defects, using parallel and convergent beams, reveal the existence of  $a[0\ 0\ 1]$  glide planes and  $n[1\ 0\ 0]$  diagonal glide planes that are incompatible with the large longitudinal displacement of the bi-stripe model. Although our study supports the Wigner-crystal model, detailed analysis suggests that, in our samples, the incommensurate charge modulation in the material has an average wave vector  $\mathbf{q}=(0.284, 0, \xi)$  with  $|\xi|=0.010$ . The symmetry breaking associated with the small component  $\xi$  along the  $c$  axis has not been previously observed by high-resolution x-ray or neutron powder diffraction.

### I. INTRODUCTION

Charge ordering in  $\text{La}_{1-x}\text{Ca}_x\text{MnO}_3$  has recently attracted much attention,<sup>1-8</sup> largely because these oxides have exciting potential practical applications due to their colossal magnetoresistance effects. Furthermore, interesting issues in physics stem from the interplay between charge ordering, orbital ordering, magnetic ordering, and transport properties. The charge-ordered state of the manganites depends delicately on the valence and local environment of the Mn cations. Since  $\text{Mn}^{3+}$  and  $\text{Mn}^{4+}$  differ significantly in size, altering their occupation sites changes the Mn-O-Mn bonding length and angle and thus the tilt of the  $\text{MnO}_6$  octahedra.

The average crystal structure of the perovskite  $\text{La}_{1-x}\text{Ca}_x\text{MnO}_3$  at room temperature (RT) has an orthorhombic symmetry with a space group of  $Pnma$ . When the temperature is lowered through a transition temperature  $T_{\text{CO}}$ , charge and orbital ordering occur. The crystallographic superstructure associated with the charge and orbital ordering in  $\text{La}_{0.5}\text{Ca}_{0.5}\text{MnO}_3$  was observed by Chen and Cheong using transmission electron microscopy (TEM).<sup>1</sup> Subsequently, a quantitative analysis was made by Radaelli *et al.* using synchrotron x-ray and neutron powder diffraction.<sup>3</sup> In later studies of superlattice reflections in the  $\text{La}_{1-x}\text{Ca}_x\text{MnO}_3$  family with  $x=0.67, 0.75$ , Chen, Cheong, and Hwang<sup>4</sup> found a linear dependence  $m=1-x$  ( $m$  being the magnitude of the modulation wave vector along the  $a$  axis). The detailed crystal and magnetic structure of the material with  $x=0.67$  was subsequently resolved by Fernandez-Diaz *et al.*<sup>7</sup> and Radaelli *et al.*<sup>8</sup> All these studies demonstrated charge, orbital, and magnetic ordering in the low-temperature  $\text{La}_{1-x}\text{Ca}_x\text{MnO}_3$  homologous series.

Knowledge of the structure of the charge-ordered phase is crucial to understanding the physical properties of these technologically important manganese perovskites. However, the discrepancy in the crystallographic superstructure of charge-ordered  $\text{La}_{0.33}\text{Ca}_{0.67}\text{MnO}_3$  derived from recent studies is striking. While Chen, Cheong, and Hwang,<sup>4</sup> Fernandez-Diaz *et al.*,<sup>7</sup> and Radaelli *et al.*<sup>8</sup> proposed a Wigner-crystal-like arrangement of the  $\text{Mn}^{3+}$  and  $\text{Mn}^{4+}$  cations with the  $\text{Mn}^{3+}$  stripes in the  $a_{\text{CO}}\text{-}c_{\text{CO}}$  plane arranged as far apart as possible [Fig. 1(a)] to minimize the Coulomb repulsion energy, Mori *et al.*<sup>5,6</sup> suggested a bi-stripe model, in which opposite orbital-ordered  $\text{Mn}^{3+}$  cations form a narrow pair of distorted  $\text{Mn}^{3+}\text{O}_6$  stripes (bi-stripes), separated by widely spaced nonpaired stripes of undistorted  $\text{Mn}^{4+}\text{O}_6$  octahedra [Fig. 1(b)] for each modulation period, irrespective of periodicity. Furthermore, Radaelli and co-workers<sup>2,3,8</sup> proposed that charge-ordering modulation is along only the  $\mathbf{a}_O$  direction with a modulation wave vector  $\mathbf{q}=(\frac{1}{3}\ 0\ 0)_O$  (subcell setting, denoted by subscript  $O$ ), Chen and co-workers<sup>1,4</sup> and Fernandez-Diaz *et al.*<sup>7</sup> suggested the modulation can be along both the  $\mathbf{a}_O$  and  $\mathbf{c}_O$  direction in a twinning-related arrangement. The displacement of the  $\text{MnO}_6$  octahedra in the models proposed by Fernandez-Diaz *et al.*<sup>7</sup> and Radaelli and co-workers<sup>3,8</sup> is predominantly transverse, while that in the model proposed by Mori *et al.*<sup>5,6</sup> is longitudinal.

Resolving these discrepancies is of the utmost importance. It is essential to be able to determine the validity of the model: Wigner-crystal or bi-stripe. Further, the apparently contradictory evidence from TEM and x-ray diffraction needs to be explained. This is important not only for manganites, but also for a wide range of transition-metal oxides, such as the nickelates and the cuprate superconductors. Identifying

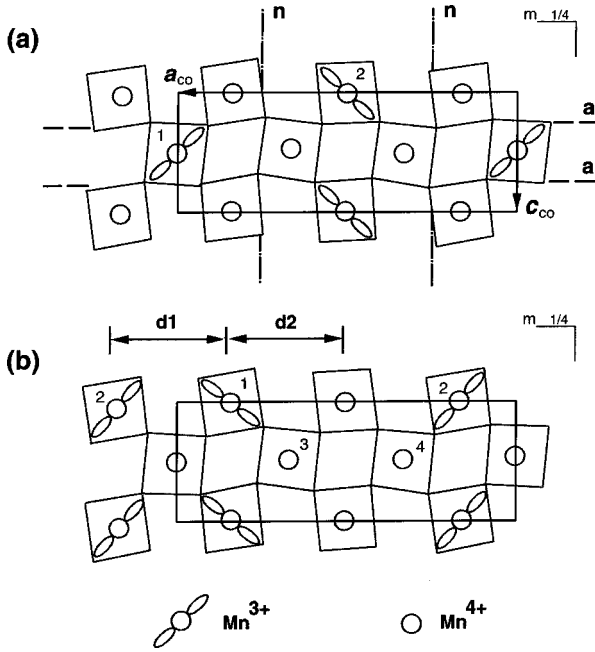


FIG. 1. Schematic projections along the  $b$  axis depicting superstructures of the charge-ordered  $\text{La}_{0.33}\text{Ca}_{0.67}\text{MnO}_3$ .  $\text{Mn}^{3+}$  and  $\text{Mn}^{4+}$  ions are shown as circles with and without orbitals, respectively. The distorted squares represent the  $\text{MnO}_6$  octahedra, and La and Ca cations are omitted. (a) The Wigner-crystal model with symmetry elements  $n[100]$ ,  $m[010]$ , and  $a[001]$ . (b) The bi-stripe model which does not have glide symmetries of  $n[100]$  and  $a[001]$ .

tying the building blocks for the charge-ordered structure is essential in understanding the fundamental physics of these materials. Recently, we took advantage of the small probe size in TEM using electron diffraction and imaging to retrieve structural information from areas far away from defects in polycrystalline  $\text{La}_{0.33}\text{Ca}_{0.67}\text{MnO}_3$ . Since  $\text{La}_{0.33}\text{Ca}_{0.67}\text{MnO}_3$  is heavily twinned with six orientational twinning variants, and has various structural defects such as grain-, twin-, and charge-ordered domain boundaries, volume-averaged structural information from x rays can be ambiguous in addressing the structure of perfect, or ideal single crystals. Here, we report our studies on evaluating the Wigner-crystal and the bi-stripe models in  $\text{La}_{0.33}\text{Ca}_{0.67}\text{MnO}_3$  by comparing our experimental observations with calculations based on the two models. We combined quantitative electron diffraction with high-resolution electron microscopy (HREM) to examine the crystal symmetry of the charge-ordered phase and the stripe spacing of  $\text{Mn}^{3+}\text{O}_6$  and  $\text{Mn}^{4+}\text{O}_6$  octahedra associated with the longitudinal and transverse displacements. Kinematical and dynamic simulations of both diffraction and images based on the two models were also performed to be compared to the experimental observations. We conclude that the Wigner-crystal model best explains our TEM results.

## II. EXPERIMENT

Polycrystalline  $\text{La}_{0.33}\text{Ca}_{0.67}\text{MnO}_3$  samples were synthesized by a solid-state reaction. The starting materials of  $\text{La}_2\text{O}_3$ ,  $\text{CaCO}_3$ , and  $\text{Mn}_3\text{O}_4$  were mixed in stoichiometric proportions and heated in air at  $1375^\circ\text{C}$  for 11 h, after thor-

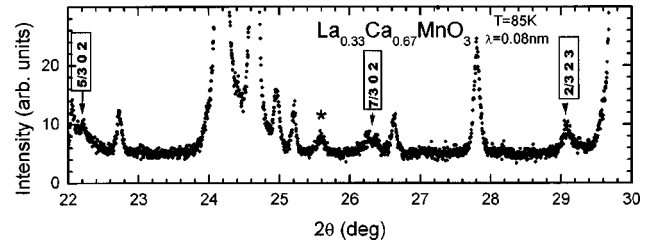


FIG. 2. High-resolution x-ray-diffraction scan at 85 K of  $\text{La}_{0.33}\text{Ca}_{0.67}\text{MnO}_3$  illustrating charge-ordering peaks, identified with arrows, similar to those observed by Radaelli *et al.*<sup>8</sup> Peak marked with asterisk is due to the copper sample holder.

ough calcination and intermediate grindings. High-resolution synchrotron powder x-ray-diffraction data were obtained at BNL National Synchrotron Light Source beamline X7A. The powdered sample was pressed onto a greased flat copper block which was then mounted in a continuously operating closed cycle helium cryostat. The diffraction setup utilized a double Si(111) monochromator with a Ge analyzing crystal. The x-ray wavelength was  $\lambda = 0.07988$  nm. A segment of the diffraction scan of the sample at a temperature  $T = 85$  K (Fig. 2) shows charge-ordering peaks very similar to those observed by Radaelli *et al.*<sup>8</sup>

TEM specimens were prepared by a standard procedure of mechanical polishing, dimpling, and ion milling. TEM experiments were conducted with a JEOL 3000F field-emission electron microscope operated at 300 kV. The *in situ* cooling experiments were carried out using a liquid- $\text{He}_2/\text{N}_2$  low-temperature stage. Utilizing liquid nitrogen, the lowest nominal temperature of the sample area is 85 K. Electron-diffraction patterns and HREM images were recorded on film negatives as well as on image plates and a charge-coupled device (CCD) camera. The latter two have a linear intensity response, and a much larger dynamic range than film negatives. For quantitative analysis, some diffraction patterns and images were energy filtered using the Gatan Imaging Filter. Calculations and simulations of HREM images and diffraction were carried out with modified Mac Tempas software and our own computer codes.

## III. RESULTS

### A. Crystal symmetry of the charge-ordered phase

We started with conventional selected area diffraction (SAD) using a parallel electron beam to examination of crystal symmetry. At room temperature,  $\text{La}_{0.33}\text{Ca}_{0.67}\text{MnO}_3$  is orthorhombic and has a lattice parameter  $a_O \cong c_O \cong \sqrt{2}a_P$ ,  $b_O \cong 2a_P$ , where  $a_O = 0.53812$  nm,  $b_O = 0.75687$  nm, and  $c_O = 0.53864$  nm, are the edge length for the orthorhombic cell and  $a_P$  for the primitive perovskite cubic cell. When temperature  $T < T_{CO}$ , a charge-ordered phase forms due to the selective occupation of  $\text{Mn}^{3+}$  and  $\text{Mn}^{4+}$  on specific sites. The charge-ordered structure has an expanded unit cell with  $a_{CO} = 3a_O$ ,  $b_{CO} = b_O$ , and  $c_{CO} = c_O$ .

The structures of the two models are sketched in Fig. 1. The major difference between the structures is the charge, and orbital ordering of the  $\text{Mn}^{3+}$  and  $\text{Mn}^{4+}$  octahedron and the associated superlattice symmetry. In Fig. 1(a), we depict

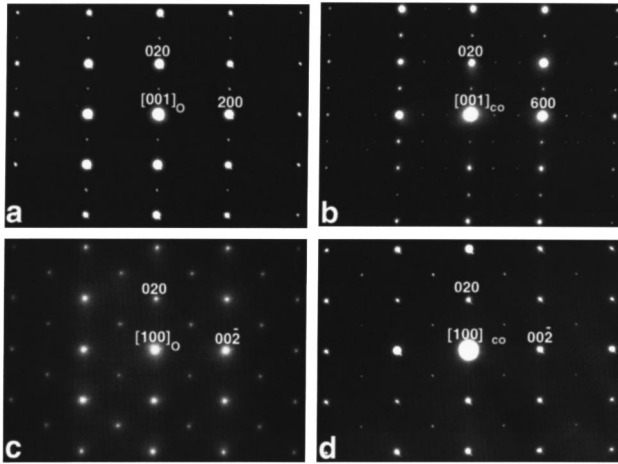


FIG. 3. Selected area diffraction patterns of  $(001)^*$  zone (a) and (b) and  $(100)^*$  zone (c) and (d) at RT and 85 K in  $\text{La}_{0.33}\text{Ca}_{0.67}\text{MnO}_3$ . (a), RT, and (b) 85 K, the extinction conditions suggest both have an  $a[001]$  glide plane. (c) RT, and (d) 85 K, the extinction conditions suggest both have a  $n[100]$  diagonal glide plane. The bracket above the transmitted spot in the figure indicates the zone axis. (a) and (c) are in subcell settings denoted by subscript  $O$ , and (b) and (d) are in supercell settings denoted by subscript  $CO$ . Note, the modulation only occurs along the  $a$  axis.

the major symmetry elements of  $n[100]$ ,  $m[010]$ , and  $a[001]$  for the space group  $Pmna$ , taken from the *International Tables for Crystallography*.<sup>9</sup> For the Wigner-crystal model, the glide  $a[001]$  operation, for example, transforms the  $\text{Mn}^{3+}$  octahedron marked as “1” into the  $\text{Mn}^{3+}$  octahedron “2,” while the diagonal glide plane  $n[100]$  transforms the  $\text{Mn}^{3+}$  octahedron “1” into the equivalent  $\text{Mn}^{3+}$  octahedron “2” but shifted  $\frac{1}{2}$  unit cell up or below along the  $b$  axis, or along the projection. For the bi-stripe model, there are no such symmetrical operations. For example, the glide  $a[001]$  would transform the  $\text{Mn}^{3+}$  octahedra 1 and 2 into the  $\text{Mn}^{4+}$  octahedra 4 and 3, respectively, while the diagonal glide  $n[100]$  operation would transform the  $\text{Mn}^{3+}$  octahedra 1 and 2 into the equivalent  $\text{Mn}^{4+}$  octahedra 3 and 4, respectively. Therefore the bi-stripe model does not have  $n[100]$  and  $a[001]$  operations although the mirror symmetry  $m[010]$  perpendicular to the  $b$  axis is retained. It is evident that the superstructure of the bi-stripe model does not belong to the  $Pmna$  space group, but has a much lower crystal symmetry with a space group of  $Pm$ .

Selected area diffraction (SAD), using a parallel electron beam combined with *in situ* cooling, was used to examine the change of crystal symmetry and the existence of the diagonal glide  $n[100]$  and glide  $a[001]$  symmetry operations in  $\text{La}_{0.33}\text{Ca}_{0.67}\text{MnO}_3$ , taken from areas of a few  $\mu\text{m}^2$ . Figure 3 shows diffraction patterns of the  $[001]_O$  and  $[001]_{CO}$  zone of  $\text{La}_{0.33}\text{Ca}_{0.67}\text{MnO}_3$  recorded at room temperature (RT) and at low temperature (LT, 85 K). Note that the subscripts  $O$  and  $CO$  refer to the index of subcell setting (RT phase) and supercell setting (charge-ordered phase), respectively. Figure 3(a), taken at RT, features an edge-length ratio of  $2\sqrt{2}$  along the  $a$  and  $b$  axis. When the temperature falls below  $T_{CO}$ , sharp weak superlattice reflections with a modulation wave vector  $\mathbf{q}=(\frac{1}{3}00)$  appear [Fig. 3(b)], indicative of the tripling of the  $a$  lattice and the charge-ordered

state. In contrast, the SAD pattern of the  $[100]$  zone, which is a face-centered rectangle, does not change with temperature, as shown in Figs. 3(c) and (d) for RT and 85 K, respectively. No super-reflections were observed below  $T_{CO}$ , even at 85 K, suggesting no charge modulation along the  $c$  axis. We studied nearly two dozen  $[011]_p$  orientated grains. Although each of them often contains more than 20 orientational domains, including twinning domains, the probability of observing the charge ordering in a  $[011]_p$  orientation of the parent phase is only  $\frac{1}{6}$ . In all cases, we found that the super-reflections only appear along the  $a^*$  axis. Thus we conclude that the charge-ordering modulation propagates only along the  $\mathbf{a}_O$ , not the  $\mathbf{c}_O$ , direction.

Despite the enlarged unit cell of the charge-ordered structure, the extinction conditions for the  $[001]$  zone pattern at RT and LT are the same, with  $h=2n$  allowed for  $(hk0)$  reflections. That is, the reflections, such as  $(100)_O$ ,  $(110)_O$ ,  $(120)_O$  are extinct, as clearly seen in Figs. 3(a) and (b). For  $(0k0)$  reflections,  $k=2n$  are allowed. The weak spots of  $(0k0)$  with  $k=\pm 1,3$  in Figs. 3(a) and (b) are due to the multiple scattering of the electron beam along the low-index zone. When we probed a thin area, and/or tilted the sample away from the low-index zone to minimize multiple scattering, the  $(0k0)$  ( $k=2n+1$ ) reflections disappeared. The forbidden rule for  $(0k0)$  reflections can be further confirmed from Figs. 3(c) and (d) where the intensity of these reflections is zero. Thus, the observed extinction conditions are consistent with the presence of an  $a[001]$  glide plane for the orthorhombic phase both at RT and in the charge-ordered state. Similarly, for the  $[100]$  zone pattern at RT and LT, for reflections  $(0k1)$ ,  $k+1=2n$  are allowed; these result from the existence of a diagonal glide plane  $n[100]$ . The SAD experiments, including observations along other major zone axes, revealed that both RT and charge-ordered  $\text{La}_{0.33}\text{Ca}_{0.67}\text{MnO}_3$  have symmetry operations  $a[001]$ ,  $m[010]$ , and  $n[100]$ , and three  $2_1$  screw axes parallel to the  $a$ ,  $b$ , and  $c$  axis, respectively. The symmetry agrees with the space group of  $Pnma$  and is consistent with the Wigner-crystal model.

The overall periodicity of the modulation of the samples was measured from SAD patterns. We most frequently observed  $a_{CO}=3a_O$ , suggesting a commensurate modulation with a tripled unit cell. In the region where the modulation is not commensurate, we found its periodicity can vary from area to area on a nanometer scale. Figure 4 is a HREM image, viewing along the  $[010]$  axis of the charge-ordered  $\text{La}_{0.33}\text{Ca}_{0.67}\text{MnO}_3$ . The dark fringes marked by arrow heads indicate the period of the superlattice with mixed periodicity of  $3a_O$  and  $4a_O$ . Figure 5 shows the corresponding SAD pattern from the same region, but a larger area. The super-reflection spots along the  $a^*$  axis suggests an incommensurate modulation with a superlattice of  $a_{CO}=3.5a_O$ , due to the mixed spacings of  $3a_O$  and  $4a_O$ . Measurements of more than a dozen  $[010]$  diffraction patterns revealed that the averaged periodicity of the incommensurate charge-ordered  $\text{La}_{0.33}\text{Ca}_{0.67}\text{MnO}_3$  is of  $a_{CO}=3.54a_O$ .

It is interesting to note that, in the samples we studied, careful analysis of the  $[010]$  zone diffraction patterns, especially those recorded on image plates, repeatedly showed that the incommensurate modulation has a small component along the  $c$  axis with a wave vector  $\mathbf{q}=(m, 0, 0+\xi)$ . A ver-

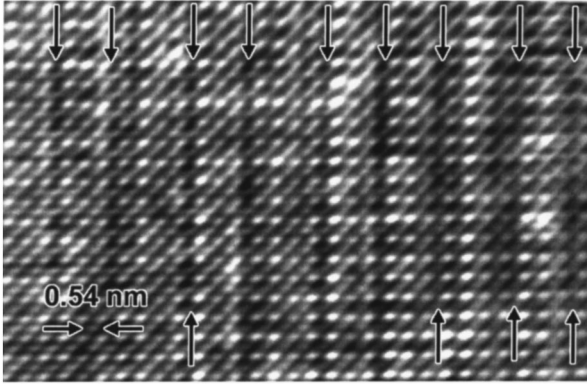


FIG. 4. HREM image of  $\text{La}_{0.33}\text{Ca}_{0.67}\text{MnO}_3$  at 85 K viewed along the  $[0\ 1\ 0]$  axis, showing the superlattice (black fringes pointed by arrowheads) with mixed  $3a_0$  and  $4a_0$  spacings.

tical shift of the neighboring super-reflections along the  $\mathbf{c}_O^*$  direction is evident. For example, Fig. 5 shows the super-reflection pairs of  $(1+m, 0, 0+\xi)$  and  $(2-2m, 0, -2\xi)$ , and  $(2+2m, 0, 2\xi)$  and  $(3-m, 0, -\xi)$ , as marked by the two pairs of arrows. Measurements reveal  $m=0.287$  and  $\xi=-0.015$ , implying that the modulation wave vector is rotated  $2.0^\circ$  away from the  $\mathbf{a}_O^*$  direction. This suggests a loss of mirror symmetry perpendicular to the  $c$  axis. The incommensurate modulation we observe has an average wave vector  $\mathbf{q}=0.284\mathbf{a}^* \pm 0.010\mathbf{c}^*$  in the subcell setting.

### B. Longitudinal and transverse displacement associated with the charge modulation

Another important approach to verify the bi-stripe model is to test the longitudinal displacement along the direction of the modulation wave vector, i.e., the  $a$  axis, for the charge-ordered  $\text{La}_{0.33}\text{Ca}_{0.67}\text{MnO}_3$ . For comparison with our experiments, we first conducted intensity calculations of  $(h\ 0\ 0)$

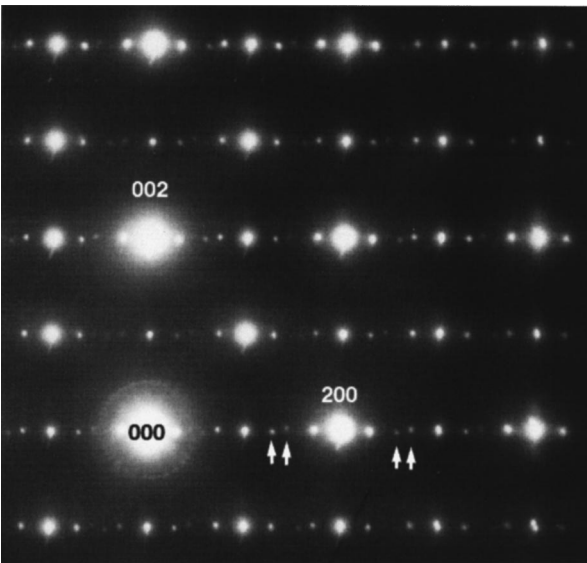


FIG. 5.  $[0\ 1\ 0]$  zone diffraction pattern at 85 K from an area including that shown in Fig. 4, revealing an incommensurate modulation with a wave vector  $\mathbf{q}=(0.284, 0, -0.010)$ . Note the modulation component along the  $\mathbf{c}_O$  direction. The average periodicity of the modulation is  $\mathbf{a}_{CO}=3.54\mathbf{a}_O$ .

reflections, based on kinematical electron-diffraction theory. We emphasized high-order reflections because they can usually be treated kinematically.<sup>10</sup> More importantly, they are sensitive to atomic position. A small displacement  $\delta\mathbf{a}_{CO}$  can alter the intensity distribution significantly for high-order reflections  $h$  due to the large value  $h\delta$  and the increasing role of the additional phase term  $2\pi h\delta$  in the structure factors of the higher-order reflections. We considered one set of lattice planes,  $(h\ 0\ 0)$ , with a displacement  $\delta$  parallel to the lattice plane normal. The unit cell consists of six atomic planes of  $\text{Mn}^{3+}$ ,  $\text{Mn}^{4+}$ , and La/Ca ions, as shown in Fig. 1(b). We set the origin at the center of the unit cell, and then added the longitudinal displacement  $-\delta/2$  and  $+\delta/2$  for the  $\text{Mn}^{4+}$  lattice planes, marked as ‘‘3’’ and ‘‘4’’ in Fig. 1(b), respectively, and  $-\delta$  and  $+\delta$  for the  $\text{Mn}^{3+}$  lattice planes, marked as ‘‘1’’ and ‘‘2,’’ respectively. Using the designation for the atomic scattering amplitude  $f^{\text{Mn}^{3+}}$  for  $\text{Mn}^{3+}$ , La/Ca lattice planes and  $f^{\text{Mn}^{4+}}$  for  $\text{Mn}^{4+}$ , La/Ca lattice planes, the structure factor of the  $(h\ 0\ 0)$  reflection  $F_{h00}$  can then be expressed as

$$F_{h00} = f^{\text{Mn}^{4+}} + 2f^{\text{Mn}^{4+}} \cos\left[2\pi h\left(\frac{1}{6} + \frac{\delta}{2}\right)\right] + 2f^{\text{Mn}^{3+}} \cos\left[2\pi h\left(\frac{2}{6} + \delta\right)\right] + f^{\text{Mn}^{4+}} \cos \pi h.$$

For fundamental reflections  $h_{CO}=6n$  with  $n$  being an integer, the structure factor  $F_{h00}$  is reduced to

$$F_{h00} = 2f^{\text{Mn}^{4+}} + 2f^{\text{Mn}^{4+}} \cos(\pi\delta h) + 2f^{\text{Mn}^{3+}} \cos(2\pi\delta h);$$

similarly, for fundamental reflections  $h=6n+3$ ,

$$F_{h00} = -2f^{\text{Mn}^{4+}} \cos(\pi\delta h) + 2f^{\text{Mn}^{3+}} \cos(2\pi\delta h).$$

For super-reflections  $h=6n\pm 1$ , the structure factor is

$$F_{h00} = 2f^{\text{Mn}^{4+}} \cos\left(\frac{(3\mp 2)\pi}{3} + \pi\delta h\right) + 2f^{\text{Mn}^{3+}} \cos\left(\frac{(3\mp 1)\pi}{3} + 2\pi\delta h\right);$$

for super-reflections  $h=6n\pm 2$ ,

$$F_{h00} = 2f^{\text{Mn}^{4+}} + 2f^{\text{Mn}^{4+}} \cos\left(\frac{(3\mp 1)\pi}{3} + \pi\delta h\right) + 2f^{\text{Mn}^{3+}} \cos\left(\frac{(3\pm 1)\pi}{3} + 2\pi\delta h\right).$$

Using these equations, envelopes of the absolute value of  $(h\ 0\ 0)$  structure factors for both fundamental ( $h=6n, 6n+3$ ) and super-reflections ( $h=6n\pm 1, 2$ ) were plotted against  $h\delta$  in Fig. 6, where  $h$  is the index of the reflections and  $\delta$  the displacement in the unit of  $\mathbf{a}_{CO}$ . We neglected the minor difference in form factors between  $\text{Mn}^{3+}$  and  $\text{Mn}^{4+}$ . In order to avoid the overall falloff of the scattering power with scattering angle, for display purpose, we normalized the structure factor  $F_{h00}$  with a constant  $f$ . Figure 6 demonstrates remarkable change in position as well as in intensity of the reflections, compared to the calculations without the dis-

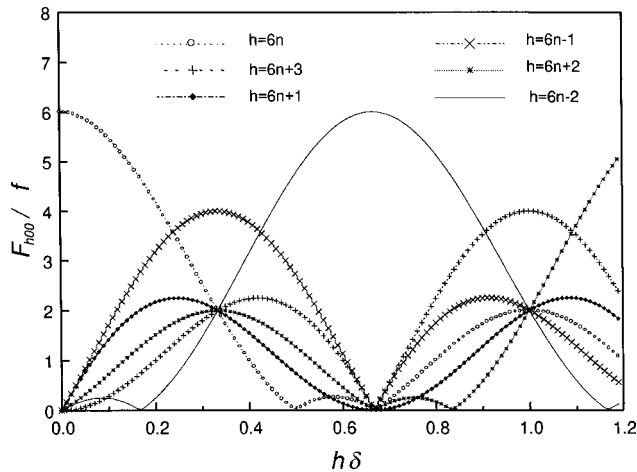


FIG. 6. Calculated intensity  $|F/f|$  of the  $(h\ 0\ 0)$  reflections ( $h = 6n, 6n \pm 1, 6n \pm 2, 6n + 3$ , where  $n$  is an integer) as a function of a hypothetical longitudinal displacement  $\delta$ , as suggested by the bi-stripe model.

placement. In the case of  $n=4\sim 5$ , i.e., for reflection  $(2400)\text{--}(3000)$ , it shows that when  $\delta=0.024$  as the case for the bi-stripe model, only the super-reflection  $(2800)$  is very strong, whereas all other reflections including fundamental reflection  $(2400)$  and  $(2700)$  are very weak, some almost vanishing due to the phase shift induced by the large longitudinal displacement. The calculations suggest a longitudinal displacement with any noticeable amplitude will significantly alter the intensity distribution among the reflections, resulting in intensities of some super-reflections being higher than those of some fundamental reflections.

To experimentally determine the intensity distribution of the charge-ordered phase, we conducted quantitative large-angle convergent electron-beam diffraction (CBED) experiments at 85 K. The advantage of CBED is that a small beam can be applied to probe a region of perfect crystal, to which perfect-crystal diffraction theory can be applied. This is particularly important for  $\text{La}_{0.33}\text{Ca}_{0.67}\text{MnO}_3$  since the material has a high density of defects. We focused on high-order reflections in regions where the thickness of the crystal is less than half the extinction lengths of all reflections at the Bragg position. Thus for  $I_1 > I_2$  we have  $|F_1| > |F_2|$  and a qualitative comparison of intensity should be feasible. To rigorously compare our experimental observations with kinematical calculations, the Gatan imaging filter attached to the microscope was used. A 10-eV energy-filtering slit was placed around the zero-loss peak of the incident beam to remove the contribution from inelastically scattered electrons, which form a background due to plasmon and other loss processes. Figure 7 is an energy-filtered CBED pattern, where we observe lines of Bragg reflections [instead of spotty pattern in SAD, Fig. 7(b)]. Off-zone-axis systematic conditions were used to minimize multiple scattering, and to collect diffraction intensities for reflections of  $(600)_O\text{--}(1200)_O$  (subcell setting), or  $(1800)_{CO}\text{--}(3600)_{CO}$  (supercell setting). Figure 7(c) shows the line scan of the intensity profile across the  $(h\ 0\ 0)$  systematic row. The intensity of the fundamental reflections follows  $I_{600} > I_{800} > I_{1000} > I_{1200}$ , partly attributable to the nonlinear decrease of atomic scattering power with the increase in scattering

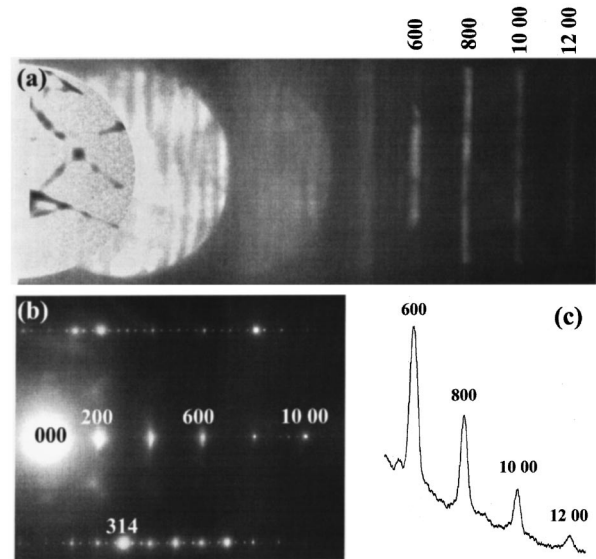


FIG. 7. (a) Off-zone-axis large-angle CBED pattern using zero-energy-loss electrons at 85 K showing lines of Bragg reflection  $(6\ 0\ 0)_O\text{--}(12\ 0\ 0)_O$  (subcell setting); (b) SAD pattern from the same area as (a) showing strong super reflections in the systematic rows of  $(h\ 14)$  and  $(h\bar{1}\ 4)$  associated with the charge ordering; (c) intensity profile corresponding to the reflections above, in (a).

angle. The super-reflections between the fundamental reflections were almost too weak to observe in the CBED pattern. Their weak intensities were reduced by the angular spread of the intensity at the Bragg position perpendicular to the corresponding reciprocal-lattice vector. However, the sharp super-reflection spots acquired from the same area along the systematic rows of  $(h\ 14)$  and  $(h\bar{1}\ 4)$  in the SAD pattern [Fig. 7(b)] confirmed that the area under investigation was indeed in a charge-ordered state. The intensities of the fundamental reflections  $(600)_O\text{--}(1200)_O$  were measured after background subtraction and are listed in Table I. They unambiguously indicated that in the reflection range we measured, all super-reflections were far weaker than the fundamental reflections. The observation contradicts the calculations (Fig. 6) based on the bi-stripe model that the intensity of a  $(h\ 0\ 0)$  super-reflection should be higher than its fundamental reflection.

To further compare our experimental observations with the bi-stripe model and Wigner-crystal model for longitudinal and transversal displacement of the  $\text{MnO}_6$  octahedra, we calculated two-dimensional SAD patterns of the  $(010)$  zone, and the structure factors of all reflections. The form factors for Ca, La, and O ions as well as for  $\text{Mn}^{3+}$  and  $\text{Mn}^{4+}$  ions were obtained from Ref. 11, atomic coordinates and Debye Waller factors from Ref. 8. We used the atomic coordinates given by Radaelli *et al.*<sup>8</sup> for the transverse displacement. For the atomic coordinates of the longitudinal bi-stripe model [Fig. 1(b)], we started from those given by Radaelli *et al.*<sup>8</sup> and then added a longitudinal wave with a displacement  $\Delta x$  onto the  $x$  coordinates of all ions. The values of the  $x$  and  $\Delta x$  associated with Mn and O shown in Fig. 1(b) are listed in Table II.

Figure 8 shows the experimental SAD pattern of the  $(010)$  zone [Fig. 8(a)], along with the calculated pattern based on the Wigner-crystal model [Fig. 8(b)] and the bi-stripe model

TABLE I. Comparison of the experimental intensities of the  $(h00)$  reflections with corresponding calculated structure factors based on the Wigner-crystal and bi-stripe models.

$(h00)_O$	$(h00)_{CO}$	$I_{\text{exp}}$	$ F^w $ (Wigner crystal)	$ F^b $ (bi-stripe)
600	1800	85	39	1.9
	1900		6.0	
	2000		1.2	
	2100		8.8	
	2200		0.7	
	2300		11.8	
800	2400	50	29	<0.5
	2500		1.0	
	2600		0.7	
	2700		1.4	
	2800		1.5	
	2900		2.0	
1000	3000	23	15	0.5
	3100		<0.5	
	3200		0.7	
	3300		2.5	
	3400		<0.3	
	3500		2.5	
1200	3600	5.6	5.3	2.6

in Fig. 8(c). We note the intensity of the reflections in a low-index zone [Fig. 8(a)] is unsuitable for quantitative analysis due to the strong multiple-scattering effects along a low-index zone axis. The advantage of such a pattern is the presence, due to the short wavelength of the electron beam, of a large number of reflections whose position can be easily identified and whose intensity can be roughly estimated. The diffraction patterns in Fig. 8 (subcell setting) consist of three types of reflections: (i) Strong fundamental spots with very high intensities forming a square network with indices  $(h0l)_O$  satisfying the diffraction conditions  $h=2n$  and  $l=2n$  with  $n$  being the integer. They are major primitive perovskite reflections with an in-phase contribution of (La, Ca) and Mn; (ii) weak fundamental spots of medium intensity with indices  $(h0l)_O$  satisfying the condition  $h=2n+1$ , or  $l=2n+1$ , and (iii) superlattice diffraction spots of weak intensity with  $h$  indices satisfying the condition  $h=n \pm \frac{1}{3}$ . The strong superlattice spots usually appear as satellites of the strong fundamental spots, but are always less intense than their fundamentals. Figure 8(b) shows, based on the Wigner-crystal model, a reasonably good match with the experimental observation [Fig. 8(a)], with the exception that some of the fundamental and super-reflections in the experiments [Fig. 8(a)] were enhanced by the multiple scattering. In contrast, the calculated pattern shown in Fig. 8(c), based on the longitudinal bi-stripe model, is incompatible with the experiment. The calculated intensities of many fundamental reflec-

tions such as those with indices  $h=4,6,8,10$  (marked by arrowheads) are much too weak compared to their satellites, while some of the satellites are much too strong. Table I lists the calculated structure factors for  $(600)_O$ - $(1200)_O$  (subcell setting), or  $(1800)_{CO}$ - $(3600)_{CO}$  (supercell setting) reflections. The calculated intensity of the fundamental reflection from the Wigner-crystal model (the reflection intensity  $I$  is proportional to the square of the corresponding structure factor  $F$ ) agrees well with the experimental measurements, for example:  $I_{1800}:I_{2400}:I_{3000}:I_{3600}=1.7:1.0:0.46:0.11$ , while  $|F_{1800}^w|^2:|F_{2400}^w|^2:|F_{3000}^w|^2:|F_{3600}^w|^2=1.8:1.0:0.29:0.33$ . On the other hand, for the bi-stripe model, we have  $I_{1800}/I_{2400} \neq |F_{1800}^b|^2/|F_{2400}^b|^2$  and  $I_{2400} \gg I_{2200}$ , but  $|F_{2400}^b|^2 \ll |F_{2200}^b|^2$ . We thus conclude that the experimental results from both CBED and SAD patterns are consistent with the Wigner-crystal model with transverse displacement, and do not agree with the bi-stripe model with the longitudinal displacement. We will further discuss the transverse displacement in Sec. IV.

### C. Stripe spacing of the $\text{Mn}^{3+}\text{O}_6$ - $\text{Mn}^{3+}\text{O}_6$ and $\text{Mn}^{3+}\text{O}_6$ - $\text{Mn}^{4+}\text{O}_6$ octahedra

The key TEM evidence upon which the longitudinal bi-stripe model was based is the difference of spacings between the stripe pairs of  $\text{MnO}_6$  octahedra along the  $a$  axis measured in TEM lattice images. Mori *et al.*<sup>5,6</sup> reported that the narrow spaced fringes, which they believe correspond to stripe distance of  $\text{Mn}^{3+}$ - $\text{Mn}^{3+}$ , marked as  $d_1$  in Fig. 9, is  $\sim 0.45$  nm, or 16%, narrower than the average lattice spacing of  $a_{CO}/3$ , and is 36% smaller than the spacing of the neighboring fringes that correspond to the in-phase  $\text{Mn}^{3+}$ - $\text{Mn}^{4+}$  stripes,  $d_2 \sim 0.65$  nm in Fig. 9. Their intensity profiles measured from the one-dimensional lattice images seemed quite convincing, although unknown crystal tilt from their images can make interpretation very difficult. If the observed variation in spacing by Mori *et al.* reflects the real charge-ordered structure of the material, how could such a large longitudinal displacement not be detected in high-resolution x-ray-diffraction experiments, since the polycrystalline samples studied by the two groups were from the same source. Previous arguments about the cause of the discrepancy focused on (i) the distinct nature of electrons and x rays in their interactions with charge-ordered crystals,<sup>12</sup> and (ii) strains in the crystals originating from structural defects,<sup>8,12</sup> such as grain boundaries, since TEM probes only local areas within a single grain while x ray probes a large volume including numerous grains and their interfaces. Nevertheless, our electron-diffraction experiments are consistent with the x-ray-diffraction observations, thus ruling out both suggested causes.

Our initial examination of the charge-ordered  $\text{La}_{0.33}\text{Ca}_{0.67}\text{MnO}_3$  in HREM mode, also revealed a distinct variation of the superlattice spacing, as reported by Mori

TABLE II.

	$\text{Mn}^{4+}$	O	$\text{Mn}^{3+}$	O	$\text{Mn}^{4+}$	O	$\text{Mn}^{4+}$	O	$\text{Mn}^{4+}$	O	$\text{Mn}^{3+}$	O
X	0	0.09	0.17	0.25	0.33	0.41	0.5	0.59	0.67	0.75	0.83	0.91
$\Delta X$	0	-0.12	-0.24	-0.18	-0.12	-0.06	0	.006	.012	.018	.024	.012

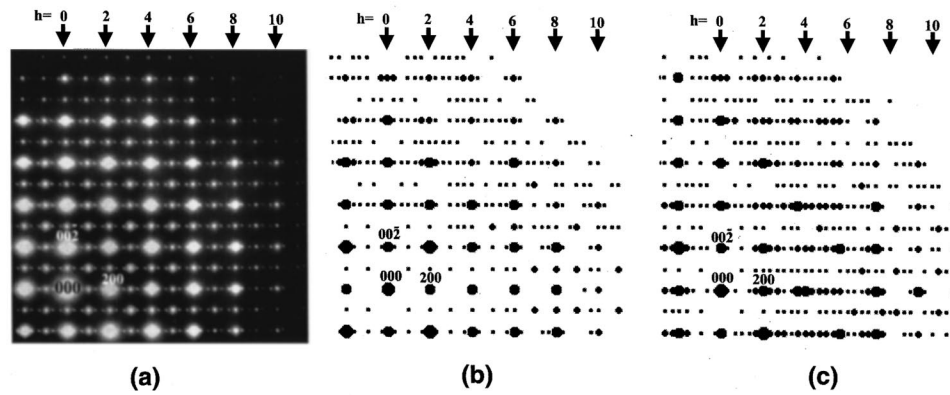


FIG. 8. Comparison between the experimental (a) and calculated [(b) and (c)] (010) diffraction patterns for charge-ordered  $\text{La}_{0.33}\text{Ca}_{0.67}\text{MnO}_3$  (subcell setting), based on (b) the Wigner-crystal model and (c) bi-stripe model. In (c), note the weak calculated intensities of many of the fundamental reflections for  $h \geq 4$ . These reduced intensities are a consequence of the predicted large longitudinal displacements of the bi-stripe model. See the text for details.

*et al.* One example is shown on the top image in Fig. 9(a). The difference in spacings between the black atom row and white atom row is apparent in the image and was confirmed by the line profile of the intensity shown in the row below in Fig. 9(a). The difference in spacing between the neighboring atomic rows measured by the intensity valleys sometimes reaches 35%, and the spacing ratio of the dark pairs and white pairs of the lattice fringes can reach 15%. Such large longitudinal displacements were not observed in electron-diffraction analysis from the same area. The discrepancy between electron diffraction and HREM motivated us to conduct extensive HREM study, mainly along the [010] zone axis with known crystal tilt and imaging conditions, of the charge-ordered  $\text{La}_{0.33}\text{Ca}_{0.67}\text{MnO}_3$  phase at 85 K.

We examined several dozen areas in exact or near [010] zone orientation and acquired hundreds of HREM images using film negatives, image plates and CCD camera with and without energy filtering. In several cases, we systematically examined the same area but made small changes in imaging conditions, e.g., beam tilting and objective lens defocusing. The details will be reported in a separate paper. In brief, we found that the superlattice images corresponding to the charge ordering usually have strong contrast in thick regions and are highly visible when the ( $h$  0 0) planes are edge on. The spacing of the superlattice, whose contrast often competes with that of the sublattice, can vary from area to area even within the same orientation variant, or twinning domain. Such variation in the images can be due to a local change of the ordered structure, but can also be due to a local change of crystal thickness and/or orientation. The superlattice spacing in images also change with imaging conditions due to microscopy aberrations, such as two- and threefold astigmatism, coma, beam alignment, and anisotropic information limit. There were many types of lattice images. We note that very different superlattice images can be observed even in neighboring areas. Very often, the details between superlattice fringes, say the  $\text{Mn}^{3+}$  and  $\text{Mn}^{4+}$  atom columns, are not well defined in the images, such as those shown in the top row of Fig. 9(b)–(d). This is in part due to the small mechanical vibration associated with the cold stage at 85 K, although their atomic spacings can be measured through image simulations. In some areas, moving through a distance of

a few nm, we observe black lattice pairs gradually becoming white lattice pairs, or vice versa, indicative of an antiphase boundary. In our study, the lattice spacing of the images was measured by the directional averaged intensity profile, as shown in the middle row of Fig. 9. Among these four types of images shown on the top row of Fig. 9, only (a) shows significant difference in spacing between the black and white atomic column rows. Such images are similar to those observed by Mori *et al.*, except Mori's are one dimensional and do not resolve atom columns. When we selectively chose images similar to Fig. 9(a) and plotted the spacing distribution as a histogram, we saw two discrete peaks in the spacing, positioned at  $d_1 = 0.49$  nm and  $d_2 = 0.59$  nm, as shown in Fig. 10(a) for 86 observations. However, plotting all the spacings (191 observations) measured from all types of images, including the other three types on the top row in Figs. 9(b)–(d) which were not reported by Mori *et al.*, we generated a different histogram with a single broad peak in spacing [Fig. 10(b)], the average value of the spacing  $d = a_{\text{CO}}/3 \approx 0.54$  nm.

To understand the origin of the variation of the images, we conducted HREM image calculations using the multislice approach based on many-beam dynamic diffraction theory. We modified the Mac Tempas computer codes taking into account the scattering amplitude of charged atoms. The electron scattering factor for  $\text{Mn}^{3+}$  and  $\text{Mn}^{4+}$  were converted from the x-ray scattering factor using the Mott formula. We carried out HREM simulations with the Wigner-crystal model only, systematically varying parameters, one at a time, by minor changes in crystal thickness, crystal orientation, defocus, beam tilt, beam divergence, centers of objective aperture, and sample drift caused by temperature fluctuations and mechanical vibration to fit experimental images. The simulation results in two unexpected findings which are consistent with experiments. First, in thin areas when the crystal was viewed in an exact [010] orientation, no superlattice with a  $3a_0$  period can be observed. Only when the crystal was thick, or was tilted away from the zone axis, was the  $3a_0$  superlattice visible. The extinction of the  $3a_0$  lattice in the exact zone axis in thin crystals is apparently due to a  $2_1$  screw axis present along the  $a$  axis. Second, under certain imaging conditions, the intensity peak of a lattice image can

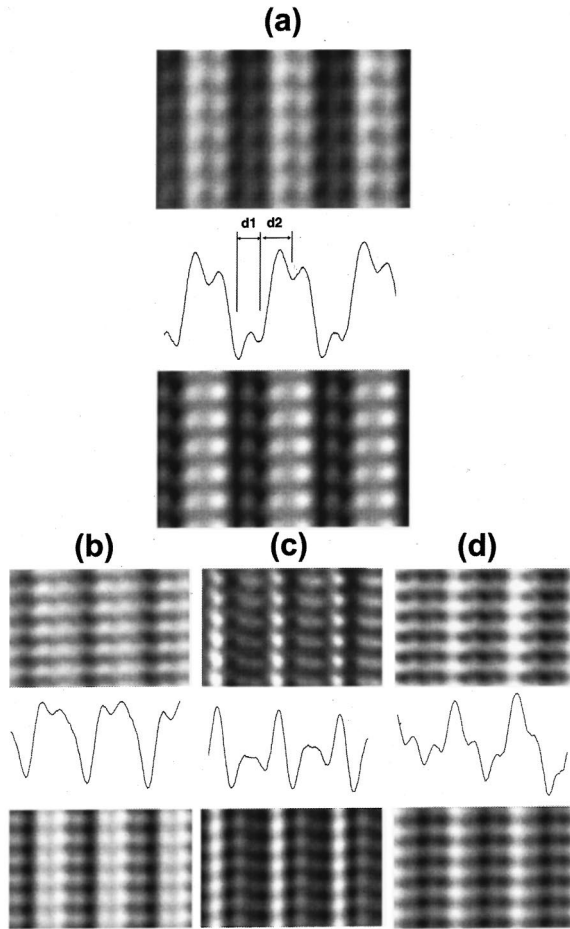


FIG. 9. Top row: four typical HREM images observed in charge-ordered  $\text{La}_{0.33}\text{Ca}_{0.67}\text{MnO}_3$  at 85 K; middle row: the corresponding intensity profiles from the images in the row above; bottom row: calculated images corresponding to the images in the top row using the Wigner-crystal model. Note the experimental image on the top of (a) is similar to that observed by Mori, Chen, and Cheong<sup>5</sup> showing narrow spacing  $d_1$ , and wide spacing  $d_2$ . A good match with the calculated image, bottom of (a) based on the Wigner-crystal model, suggests the observed variation in spacing does not require a longitudinal displacement in the structure. Parameters used in the simulation: (a)  $t = 30$  nm,  $\Delta f = -40$  nm, crystal tilt:  $h = 10$  mrad,  $l = 3.5$  mrad; (b)  $t = 10$  nm,  $\Delta f = -40$  nm, crystal tilt:  $h = 10$  mrad,  $l = 7$  mrad; (c)  $t = 70$  nm,  $\Delta f = -160$  nm, crystal tilt:  $h = 10$  mrad,  $l = 7$  mrad, (d)  $t = 20$  nm,  $\Delta f = -200$  nm, crystal tilt:  $h = 10$  mrad,  $l = 7$  mrad. In all the simulations, an objective aperture radius  $0.7 \text{ \AA}^{-1}$  centered at  $h = l = 0$  was used.

deviate far away from its actual atomic position, as indicated by the calculated image shown at the bottom of Fig. 9(a). In other words, an equally spaced periodical lattice potential can give rise to unequal spacing in lattice fringes. For  $a_{\text{CO}} = 3a_0 = 1.62$  nm superlattice structure from the Wigner-crystal model, we can observe a superlattice with a fringe period of  $a_{\text{CO}}/2 = 0.81$  nm, which corresponds to the spacing of  $\text{Mn}^{3+}\text{O}_6$  stripes, and even a period of sublattice  $a_0 = 0.54$  nm with invisible superlattice fringes, especially when the Laue center is off the origin. At present, we cannot single out any one parameter that dominates the change of the fringe spacing in lattice images. It is a combined effect. Since most of the parameters are correlated, image simulation is invaluable in interpreting such HREM images. The

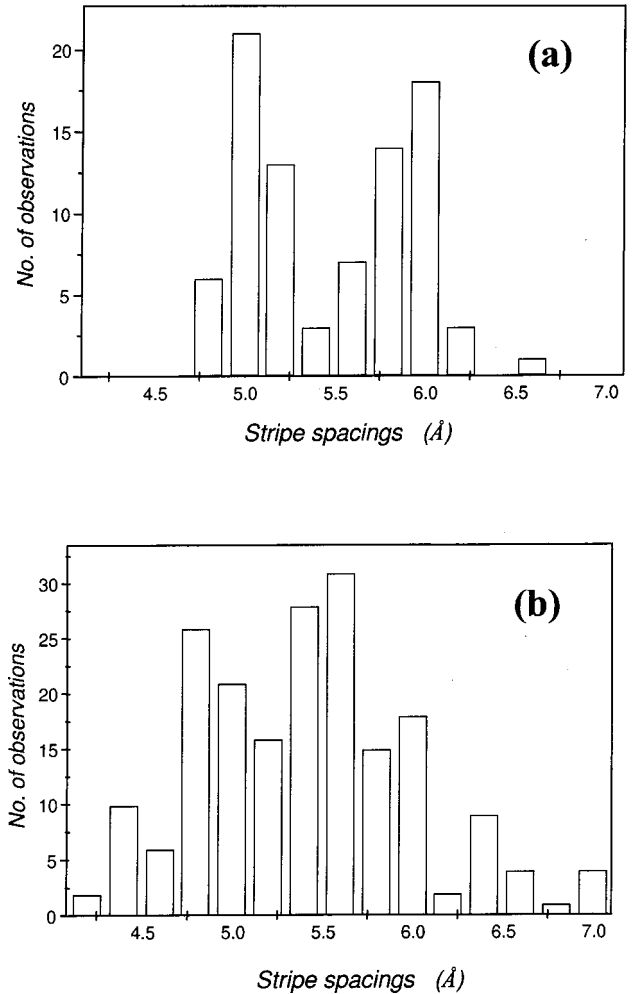


FIG. 10. Histograms of the fringe spacings, measured from HREM images of the charge-ordered phase. (a) plotted using only the type of images shown in Fig. 9(a); (b) plotted using all types of images.

four images of the bottom row in Fig. 9, which correspond to the experimental images and line scans in the rows above, are all calculated ones using the Wigner-crystal model. We conclude that even without longitudinal displacement, images with narrow and wide spaced fringes, suggested by the bi-stripe model, can also be obtained.

#### IV. DISCUSSION

Simulations of HREM images suggest that the apparent lattice spacing of the superlattice of charge-ordered  $\text{La}_{0.33}\text{Ca}_{0.67}\text{MnO}_3$  is very sensitive to crystal thickness, orientation, and other imaging conditions. Thus a small misorientation of the crystal foil may cause an extra intensity modulation in HREM image of polytypes.<sup>13</sup> It was also demonstrated experimentally and theoretically that even crystallographically forbidden lattice fringes, such as those corresponding to (010) reflections in  $\text{La}_{1-x}\text{Ca}_x\text{MnO}_3$ , can be easily obtained in HREM images,<sup>14</sup> due to broken symmetry in the diffraction process (mainly crystal tilt), or in the non-linear imaging process. Thus, without knowing crystal tilt and the experimental imaging conditions and without image simulations, it is difficult, if not impossible, to derive an

atomic structure, including coordinates, from an HREM image for a complicated materials such as charge-ordered  $\text{La}_{1-x}\text{Ca}_x\text{MnO}_3$ . Measuring lattice spacing is more straightforward in reciprocal space. However, electron diffraction is prone to multiple scattering and other dynamic effects, so care should be taken in interpreting the observations. Off-zone-axis electron diffraction in thin areas can minimize multiscattering; combining experimental data with simulations therefore is recommended. In contrast, interpreting x-ray diffraction is less complicated due to the negligible dynamic effects and multiple scattering. However, because of its large probe size, x-ray diffraction often retrieves volume-averaged structural information, and thus may misdiagnose crystal symmetry on a submicrometer scale. Since x-ray and electron diffraction are complementary techniques, the combined use of the two can usually eliminate their respective ambiguities.

It should be noted that the superlattice reflections of the ordered  $\text{La}_{1-x}\text{Ca}_x\text{MnO}_3$  at low temperature observed with high-resolution x-ray and electron diffraction is not direct evidence to the charge ordering, but evidence for the existence of displacement that may be associated with the charge. The difference in form factor alone between  $\text{Mn}^{3+}$  and  $\text{Mn}^{4+}$  is not sufficient to result in superlattice reflections. To explain the structural modulation, a transverse displacement associated with  $\text{Mn}^{3+}$  and  $\text{Mn}^{4+}$  ordering was implemented in the Wigner-crystal model. Although our TEM study rejects the longitudinal displacement in the bi-stripe mode, a transverse displacement can still exist. In Fig. 7(b), we clearly observe that the super-reflections with  $h' = h \pm \frac{2}{3}$  (subcell setting) for  $l = \pm 4$  are much stronger than the super-reflections with the same  $h'$ -indices for  $l = 0$ , suggesting the existence of a displacement along the  $c$  axis. To quantify such a displacement for the bi-stripe model, we added a sine wave as the transverse displacement along the  $c$  axis into the model with  $\Delta z = A_i \sin(2\pi x)$  ( $i = \text{La/Ca, Mn, Op, and Oa}$  with  $A_i$  being largest for  $\text{Op}$  and smallest for  $\text{Mn}$ ). We then compared the calculations with experiments. However, our observations were inconclusive for two reasons. (i) The possible displacement along the  $c$  axis is very small. Since the bi-stripe mode did not provide atomic coordinates, we used the atomic coordinates given by Radaelli *et al.*<sup>8</sup> By comparing the atomic position at 160 K for the averaged structure and charge-ordered structure we found the maximum amplitude of the transverse displacement is more than ten times smaller than the longitudinal displacement proposed by the bi-stripe model. (ii) The sensitivity in detecting the displacement along the  $c$  axis is low. The transverse displacement changes the intensity and position of the (001) reflections. However, due to the lack of superlattice reflections along the  $c^*$  axis, the widely spaced (001) reflections do not respond sensitively to a small displacement. Further study is needed

to address the transverse displacement of the charge-ordered phase.

On the other hand, the observation of incommensurate modulation with the small component  $\xi$  along the  $c$  axis in local areas is very interesting, particularly as it has not been observed by x-ray diffraction. It likely reflects the charge-ordered structure at submicrometer scale. The intensity and position, including the sign of the  $\xi$  component, of the super reflections associated with the incommensurate modulation can change with temperature, suggesting their configuration may be metastable. During *in situ* heating, we found the shape of the superreflections also changes, from strong sharp spots at well below  $T_{\text{CO}}$  ( $\sim 260$  K), to weak diffused streaks along the  $a^*$  axis at  $T_c$ , and disappear at above  $T_{\text{CO}}$ . In regions about  $0.2 \mu\text{m}$  in diameter defined by the size of SAD aperture, where the  $\xi$  component is clearly visible, we observe high density of antiphase domain boundaries. The antiphase boundaries have a very broad width as those observed for  $\text{Bi}_2\text{Sr}_2\text{CaCu}_2\text{O}_{8+\delta}$  superconductors.<sup>15</sup> Dark-field images using the superlattice reflections show that the superlattices often take a wavy form when they cross the domain boundaries. The antiphase domain has an average size of 16 nm. The shift of 0.54 nm of the  $a$  lattice across the boundaries and the domain size of 16 nm observed in HREM, is consistent with the  $\sim 2^\circ$  tilt away from the  $a_0$  axis, observed in diffraction. The  $\xi$  component can take either sign, and its magnitude varies with location of the samples, ranging from  $|\xi| = 0 \sim 0.015$ . Thus, for a large area, the size of hundreds of  $\mu\text{m}$ , the contribution of the  $c$  component  $\xi$  to x-ray diffraction may cancel out. A similar small component resulting in broken modulation symmetry observed in electron diffraction but not in high-resolution synchrotron x ray was reported by a Houston group for  $\text{Bi}_2\text{Sr}_2\text{CaCu}_2\text{O}_{8+\delta}$ .<sup>16</sup>

In conclusion, we studied charge-ordered  $\text{La}_{0.33}\text{Ca}_{0.67}\text{MnO}_3$  using TEM to retrieve single-crystal-like structural information from small areas, rather than volume-averaged structural information as by x-ray diffraction. Two conflicting structural models, the Wigner-crystal and bi-stripe models, were tested by experimental and calculated electron diffraction patterns, as well as by HREM images. Our observations are not consistent with the bi-stripe model, and support the Wigner-crystal model. Detailed TEM analysis suggests that the charge modulation on a submicron scale may have a small component along the  $c$  axis, which may not be revealed by x-ray and neutron diffraction.

#### ACKNOWLEDGMENTS

The authors would like to thank C. H. Chen and D. E. Cox for useful discussions. This work was supported by Division of Materials Sciences, U.S. Department of Energy, under Contract No. DE-AC02-98CH10886. The National Synchrotron Light Source is also supported by the U.S. Dept. of Energy, Division of Materials Sciences.

\*Author to whom correspondence should be addressed. FAX (631) 344-4071. Electronic address: zhu@bnl.gov

<sup>1</sup>C. H. Chen and S-W. Cheong, Phys. Rev. Lett. **76**, 4042 (1996).

<sup>2</sup>P. G. Radaelli, D. E. Cox, M. Marezio, S-W. Cheong, P. E. Schiffer, and A. P. Ramirez, Phys. Rev. Lett. **75**, 4488 (1995).

<sup>3</sup>P. G. Radaelli, D. E. Cox, M. Marezio, and S-W. Cheong, Phys. Rev. B **55**, 3015 (1997).

<sup>4</sup>C. H. Chen, S-W. Cheong, and H. Y. Hwang, J. Appl. Phys. **81**, 4326 (1997).

<sup>5</sup>S. Mori, C. H. Chen, and S-W. Cheong, Nature (London) **392**, 473 (1998).

<sup>6</sup>S. Mori, C. H. Chen, and S-W. Cheong, Phys. Rev. Lett. **81**, 3972 (1998).

<sup>7</sup>M. T. Fernandez-Diaz, J. L. Martinez, J. M. Alonso, and E. Her-

- tero, Phys. Rev. B **59**, 1277 (1999).
- <sup>8</sup>P. G. Radaelli, D. E. Cox, L. Capogna, S-W. Cheong, and M. Marezio, Phys. Rev. B **59**, 14 440 (1999).
- <sup>9</sup>*International Tables for Crystallography*, edited by T. Hahn (D. Reidel, Dordrecht, Holland, 1983), Vol. A.
- <sup>10</sup>J. Tafto and T. H. Metzger, J. Appl. Crystallogr. **18**, 110 (1985).
- <sup>11</sup>P. A. Doyle and P. S. Turner, Acta Crystallogr., Sect. A: Cryst. Phys., Diffr., Theor. Gen. Crystallogr. **24**, 390 (1968); D. Rez, P. Rez, and I. Grant, Acta Crystallogr., Sect. A: Found. Crystallogr. **50**, 481 (1994).
- <sup>12</sup>C. H. Chen and S.-W. Cheong (private communication).
- <sup>13</sup>W. Coene, H. Bender, F. C. Lovey, D. Van Dyck, and S. Amelinckx, Phys. Status Solidi A **87**, 483 (1985).
- <sup>14</sup>H. W. Zandbergen and J. Jansen, Ultramicroscopy **80**, 59 (1990).
- <sup>15</sup>Y. Zhu and J. Tafto, Philos. Mag. A **74**, 307 (1996).
- <sup>16</sup>X. B. Kan, J. Kulik, P. C. Chow, S. C. Moss, Y. F. Yan, J. H. Wang, and Z. X. Zhao, J. Mater. Res. **5**, 731 (1999).